Explicit finite-difference vector beam propagation method based on the iterated Crank–Nicolson scheme

Traianos V. Yioultsis, Giannis D. Ziogos, and Emmanouil E. Kriezis*

Department of Electrical and Computer Engineering, Aristotle University of Thessaloniki, GR-54124 Thessaloniki, Greece
**Corresponding author: mkriezis@auth.gr*

Received May 22, 2009; revised August 19, 2009; accepted August 21, 2009; posted August 21, 2009 (Doc. ID 111748); published September 16, 2009

We introduce and develop a new explicit vector beam propagation method, based on the iterated Crank–Nicolson scheme, which is an established numerical method in the area of computational relativity. The proposed approach results in a fast and robust method, characterized by simplicity, efficiency, and versatility. It is free of limitations inherent in implicit beam propagation methods, which are associated with poor convergence or uneconomical use of memory in the solution of large sparse linear systems, and thus it can tackle problems of considerable size and complexity. The advantages offered by this approach are demonstrated by analyzing a multimode interference coupler and a twin-core photonic crystal fiber. A possible wide-angle generalization is also provided. © 2009 Optical Society of America

OCIS codes: 00.4430, 130.2790, 130.0130, 060.5295.

1. INTRODUCTION

The beam propagation method (BPM) is considered one of the leading computational methods for the analysis of integrated photonic devices and fiber-based components. A considerable range of methodologies and formulations is reported in the literature, depending on the physics of the problem under investigation. A particularly interesting area of research is the application of vectorial BPM (VBPM) formulations for the study of optical waveguides and components that exhibit significant polarization dependence and coupling phenomena [1–3]. The overwhelming majority of finite difference (FD) and finite-element-based (FE) BPMs [4–6] rely on implicit schemes, which may render their application to problems of larger scale prohibitive, especially if memory requirements necessitate the use of iterative solvers to deal with the solution of the linear system at each step of the BPM algorithm. On the other hand, explicit techniques are very appealing, as they can extend BPM applicability to problems of larger physical scale; in addition, they easily allow for parallel implementations. However, they seem to be severely affected by stability issues or poor accuracy.

In general, the number of explicit schemes available in the BPM literature is rather limited. Such schemes could be broadly classified into earlier, conditionally stable explicit FD algorithms relying on central axial differences [7–9] and schemes based on the DuFort–Frankel method [10–12]. The latter class of methods is unconditionally stable and second-order accurate. In particular, [12] presents a proper modification to account for long-term instability problems. It seems, though, that the inherent inconsistency of the DuFort–Frankel scheme [11] not only downgrades its accuracy to the first order but also plagues the solution with spurious artifacts.

In search of an efficient explicit VBPM approach, a powerful technique appears to be the iterated Crank–Nicolson (ICN) scheme, which comes from the area of computational relativity and is well suited to the numerical treatment of parabolic differential equations. It has been suggested by Choptuik that the well-known Crank–Nicolson (CN) method can actually be replaced by an iterated scheme [13]. This has been done very successfully over the past years in solving Einstein's equations for general relativity. The ICN method has become one of the dominant approaches to solve problems of black-hole collisions, star formation, gravitational collapse, and other cosmological scenarios, which are problems of such a tremendous computational scale that they render any kind of method that employs a sparse system solution impractical. The primary merit of this technique is that the system solution at each step of the usual CN method is replaced by a simple iteration, involving only sparse matrix multiplications. The price that one has to pay is that the iterative technique is no longer unconditionally stable, and therefore the step size has to be chosen according to a stability condition. However, stability analysis shows that exactly two iterations per step and no more are necessary [13,14], while the iterative scheme fully retains its second-order accuracy.

In this paper, we propose a fully explicit vector BPM approach, based on the ICN method. A vectorial formulation has been chosen to account for a broad range of devices, as typically anticipated in state-of-the-art photonic technology. A step-by-step derivation of the underlying formulation and its numerical implementation via the ICN scheme is thoroughly presented in Section 2. A route to the construction of wide-angle variants is discussed in Section 3. A class of diverse large-scale problems are tar-

geted in Section 4, in particular, a 1×4 multimode interference coupler, a twin-core photonic crystal fiber coupler, and also a tilted ridge waveguide for evaluating wide-angle propagation. Extensive validation and assessment of the proposed scheme are carried out with respect to other well-established VBPM techniques.

2. FORMULATION

The development of the VBPM is based on the vector wave equation for isotropic media,

$$\nabla\times\nabla\times\mathbf{E}-k_0^2n^2\mathbf{E}=\mathbf{0}, \tag{1}$$

which is equivalently written as

$$\nabla^2\mathbf{E}+k_0^2n^2\mathbf{E}-\nabla(\nabla\cdot\mathbf{E})=\mathbf{0}. \tag{2}$$

In Eq. (2) $n=n(x,y,z)$ is the index of refraction, which is assumed to vary slowly along the main propagation axis z. Under the assumption $\partial n^2/\partial z\approx0$ and taking into account the zero divergence of the electric flux density, $\nabla\cdot(n^2\mathbf{E})=0$, the vector formulation (2) is decomposed into the following three scalar equations:

$$\nabla^2E_x+\frac{\partial}{\partial x}\left[\frac{1}{n^2}\frac{\partial}{\partial x}(n^2E_x)\right]+\frac{\partial}{\partial x}\left[\frac{1}{n^2}\frac{\partial}{\partial y}(n^2E_y)\right]-\frac{\partial^2E_x}{\partial x^2}-\frac{\partial^2E_y}{\partial x\partial y}+k_0^2n^2E_x=0, \tag{3a}$$

$$\nabla^2E_y+\frac{\partial}{\partial y}\left[\frac{1}{n^2}\frac{\partial}{\partial y}(n^2E_y)\right]+\frac{\partial}{\partial y}\left[\frac{1}{n^2}\frac{\partial}{\partial x}(n^2E_x)\right]-\frac{\partial^2E_y}{\partial y^2}-\frac{\partial^2E_x}{\partial y\partial x}+k_0^2n^2E_y=0, \tag{3b}$$

$$\nabla^2E_z+\frac{\partial}{\partial z}\left[\frac{1}{n^2}\frac{\partial}{\partial x}(n^2E_x)\right]+\frac{\partial}{\partial z}\left[\frac{1}{n^2}\frac{\partial}{\partial y}(n^2E_y)\right]-\frac{\partial^2E_x}{\partial z\partial x}-\frac{\partial^2E_y}{\partial z\partial y}+k_0^2n^2E_z=0. \tag{3c}$$

The above equations are exact for optical devices that are uniform along the propagation axis z but are also considered fairly accurate for the cases where the longitudinal variation is sufficiently small compared with the transverse one. To develop the BPM, one has to express the electric field as the product of a fast-varying reference phase term and a spatial field envelope $\tilde{\mathbf{E}}$,

$$\mathbf{E}=\tilde{\mathbf{E}}\exp(-jk_{\mathrm{ref}}z), \tag{4}$$

where $k_{\mathrm{ref}}=k_0n_{\mathrm{ref}}$ and n_{ref} is an arbitrarily chosen reference refractive index. Substituting Eq. (4) into Eqs. (3) and applying the paraxial approximation, i.e., $|\partial^2\tilde{\mathbf{E}}/\partial z^2|\ll2k_{\mathrm{ref}}|\partial\tilde{\mathbf{E}}/\partial z|$, the second-order derivative term of the field envelope with respect to z is dropped, and the paraxial envelope vector equations are written in compact form as

$$\frac{\partial}{\partial z}\left\{\begin{bmatrix}\tilde{E}_x\\ \tilde{E}_y\end{bmatrix}\right\}=\begin{bmatrix}A_{xx} & A_{xy}\\ A_{yx} & A_{yy}\end{bmatrix}\begin{bmatrix}\tilde{E}_x\\ \tilde{E}_y\end{bmatrix}, \tag{5a}$$

$$\frac{\partial\tilde{E}_z}{\partial z}=A_{zz}\tilde{E}_z+B(\tilde{E}_x,\tilde{E}_y), \tag{5b}$$

where the differential operators A_{xx}, A_{xy}, A_{yx}, A_{yy}, A_{zz}, B are defined as

$$A_{xx}\tilde{E}_x=\frac{1}{j2k_{\mathrm{ref}}}\left\{\frac{\partial}{\partial x}\left[\frac{1}{n^2}\frac{\partial}{\partial x}(n^2\tilde{E}_x)\right]+\frac{\partial^2\tilde{E}_x}{\partial y^2}+k_0^2(n^2-n_{\mathrm{ref}}^2)\tilde{E}_x\right\}, \tag{6a}$$

$$A_{xy}\tilde{E}_y=\frac{1}{j2k_{\mathrm{ref}}}\left\{\frac{\partial}{\partial x}\left[\frac{1}{n^2}\frac{\partial}{\partial y}(n^2\tilde{E}_y)\right]-\frac{\partial^2\tilde{E}_y}{\partial x\partial y}\right\}, \tag{6b}$$

$$A_{yx}\tilde{E}_x=\frac{1}{j2k_{\mathrm{ref}}}\left\{\frac{\partial}{\partial y}\left[\frac{1}{n^2}\frac{\partial}{\partial x}(n^2\tilde{E}_x)\right]-\frac{\partial^2\tilde{E}_x}{\partial y\partial x}\right\}, \tag{6c}$$

$$A_{yy}\tilde{E}_y=\frac{1}{j2k_{\mathrm{ref}}}\left\{\frac{\partial}{\partial y}\left[\frac{1}{n^2}\frac{\partial}{\partial y}(n^2\tilde{E}_y)\right]+\frac{\partial^2\tilde{E}_y}{\partial x^2}+k_0^2(n^2-n_{\mathrm{ref}}^2)\tilde{E}_y\right\}, \tag{6d}$$

$$A_{zz}\tilde{E}_z=\frac{1}{j2k_{\mathrm{ref}}}\left[\frac{\partial^2\tilde{E}_z}{\partial x^2}+\frac{\partial^2\tilde{E}_z}{\partial y^2}+k_0^2(n^2-n_{\mathrm{ref}}^2)\tilde{E}_z\right], \tag{6e}$$

$$B(\tilde{E}_x,\tilde{E}_y)=\frac{1}{j2k_{\mathrm{ref}}}\left(\frac{\partial}{\partial z}-jk_{\mathrm{ref}}\right)\left[\frac{1}{n^2}\frac{\partial}{\partial x}(n^2\tilde{E}_x)+\frac{1}{n^2}\frac{\partial}{\partial y}(n^2\tilde{E}_y)-\frac{\partial\tilde{E}_x}{\partial x}-\frac{\partial\tilde{E}_y}{\partial y}\right]. \tag{6f}$$

The above differential operators, when discretized by finite differences in the transverse plane, are equivalent to sparse matrices $\mathbf{A}_t$, $\mathbf{A}_z$, and $\mathbf{B}$. All differential operators are treated via the usual central finite differences, as extensively discussed in the related literature; see for instance [2]. Therefore, Eqs. (5) are cast in matrix form as

$$\frac{\partial}{\partial z}\tilde{\mathbf{E}}_t=\mathbf{A}_t\tilde{\mathbf{E}}_t, \tag{7a}$$

$$\frac{\partial}{\partial z}\tilde{\mathbf{E}}_z=\mathbf{A}_z\tilde{\mathbf{E}}_z+\mathbf{B}\tilde{\mathbf{E}}_t, \tag{7b}$$

where $\tilde{\mathbf{E}}_t$ is a column vector comprising the nodal values of the x and y components of the electric field envelope and the column vector $\tilde{\mathbf{E}}_z$ contains the nodal values of the axial component.

Equations (7) are typically solved via an implicit CN scheme, which is unconditionally stable provided that its weight parameter varies within the interval [0.5,1]. However, the implicit nature of the scheme demands appreciable computational resources, especially for large-scale three-dimensional problems, as a sparse linear system needs to be solved in every propagation step. A promising alternative is to replace the implicit CN scheme with an equivalent iterated version [13,14]. This will effectively transform the implicit technique into an explicit one.

Theoretically, the ICN scheme converges to the implicit one in an infinite number of iterations per step; however, a very limited number of iterations is sufficient to guarantee second-order accuracy. Stability analysis suggests that the smallest possible number of iterations is equal to two [13]. Contrary to the conventional CN scheme, which is unconditionally stable, the ICN is restricted to axial (propagation) steps that are below a limiting threshold.

We present the implementation of the ICN scheme in the following steps. The transverse electric field Eq. (7a) is treated first. The iteration starts by calculating a first approximation $^{(1)}\tilde{\mathbf{E}}_t^{l+1}$ of the transverse field at the next propagation plane $l+1$ by discretizing Eq. (7a) using forward finite differences:

$$\frac{^{(1)}\tilde{\mathbf{E}}_t^{l+1}-\tilde{\mathbf{E}}_t^{l}}{\Delta z}=\mathbf{A}_t\tilde{\mathbf{E}}_t^{l}. \tag{8}$$

Advancing the field using only Eq. (8) would correspond to the well-known first-order explicit Euler scheme. Then, an estimate of the field at the midstep plane $(l+1/2)$ is formed by averaging:

$$^{(1)}\tilde{\mathbf{E}}_t^{l+1/2}=a_1\,^{(1)}\tilde{\mathbf{E}}_t^{l+1}+(1-a_1)\tilde{\mathbf{E}}_t^{l}, \tag{9}$$

where a_1 is the ICN weight parameter, analogous to the weight parameter of the conventional CN scheme. Similarly, a second iteration provides a new estimate of the field at the next propagation plane $l+1$,

$$\frac{^{(2)}\tilde{\mathbf{E}}_t^{l+1}-\tilde{\mathbf{E}}_t^{l}}{\Delta z}=\mathbf{A}_t\,^{(1)}\tilde{\mathbf{E}}_t^{l+1/2}, \tag{10}$$

while a next improved midstep value is obtained by averaging:

$$^{(2)}\tilde{\mathbf{E}}_t^{l+1/2}=a_2\,^{(2)}\tilde{\mathbf{E}}_t^{l+1}+(1-a_2)\tilde{\mathbf{E}}_t^{l}. \tag{11}$$

In general, the ICN weight parameters a_1 and a_2 could be different. In most cases the weight parameters are naturally selected equal to 1/2, and this practice is followed throughout this paper. Finally, the iteration is completed by the final estimate of the next plane field:

$$\frac{\tilde{\mathbf{E}}_t^{l+1}-\tilde{\mathbf{E}}_t^{l}}{\Delta z}=\mathbf{A}_t\,^{(2)}\tilde{\mathbf{E}}_t^{l+1/2}. \tag{12}$$

If one wishes to establish a direct relation between fields at two consecutive transverse planes, without the aid of the above intermediate steps, it can be easily proved that Eqs. (8)–(12) are equivalent to

$$\tilde{\mathbf{E}}_t^{l+1}=[\mathbf{I}+\Delta z\mathbf{A}_t+a_2(\Delta z\mathbf{A}_t)^2+a_1a_2(\Delta z\mathbf{A}_t)^3]\tilde{\mathbf{E}}_t^{l}. \tag{13}$$

However, we stress that throughout this paper the field updates are performed according to Eqs. (8)–(12). Although it is equivalent to apply Eq. (13) explicitly, this might give the misleading impression that one has to directly compute the denser matrices $\mathbf{A}_t^2,\mathbf{A}_t^3$, which would result in a less efficient scheme in terms of memory management. In order to apply Eq. (13), matrix powers should be indirectly calculated via matrix-vector products of the form $\mathbf{A}_t^n\tilde{\mathbf{E}}_t^l=\mathbf{A}_t^{n-1}(\mathbf{A}_t\tilde{\mathbf{E}}_t^l)$.

In a similar way, the axial component $\tilde{E}_z$ will be calculated by implementing two ICN iterations in Eq. (7b), using the already available values of the column vector $\tilde{\mathbf{E}}_t$:

$$\frac{^{(1)}\tilde{\mathbf{E}}_z^{l+1}-\tilde{\mathbf{E}}_z^{l}}{\Delta z}=\mathbf{A}_z\tilde{\mathbf{E}}_z^{l}+\mathbf{B}\tilde{\mathbf{E}}_t^{l+1/2}, \tag{14}$$

$$^{(1)}\tilde{\mathbf{E}}_z^{l+1/2}=a_1\,^{(1)}\tilde{\mathbf{E}}_z^{l+1}+(1-a_1)\tilde{\mathbf{E}}_z^{l}, \tag{15}$$

$$\frac{^{(2)}\tilde{\mathbf{E}}_z^{l+1}-\tilde{\mathbf{E}}_z^{l}}{\Delta z}=\mathbf{A}_z\,^{(1)}\tilde{\mathbf{E}}_z^{l+1/2}+\mathbf{B}\tilde{\mathbf{E}}_t^{l+1/2}, \tag{16}$$

$$^{(2)}\tilde{\mathbf{E}}_z^{l+1/2}=a_2\,^{(2)}\tilde{\mathbf{E}}_z^{l+1}+(1-a_2)\tilde{\mathbf{E}}_z^{l}, \tag{17}$$

$$\frac{\tilde{\mathbf{E}}_z^{l+1}-\tilde{\mathbf{E}}_z^{l}}{\Delta z}=\mathbf{A}_z\,^{(2)}\tilde{\mathbf{E}}_z^{l+1/2}+\mathbf{B}\tilde{\mathbf{E}}_t^{l+1/2}. \tag{18}$$

It should be noted that the value of the transverse field at the midstep plane involved in Eqs. (14), (16), and (18) is simply the average value between planes l and $l+1$.

The explicit manner of the proposed formulation eliminates the need for solving a sparse linear system at each propagation step, which is the case in all implicit schemes. However, the ICN scheme is no longer unconditionally stable, and stability analysis results in a constraint for the maximum allowed step size. In fact, the maximum axial propagation step Δz depends on the transverse cell size Δx, Δy, and it is typically found to be smaller than in the case of an implicit scheme; however, it will be proved that this is not restrictive, since the computational effort per propagation step is found to be minimal in our approach. In particular, the amount of computational effort per propagation step corresponds to three matrix-vector multiplications, as opposed to the single matrix-vector multiplication involved in other explicit schemes. However, the latter ones are only first-order accurate, a fact that has a great impact on the solution accuracy. It is stressed that our scheme is second order, and thus all comparisons are performed against the second-order accurate CN scheme. In Section 4 it will be demonstrated that the overall gain in computation speed is significant despite the increase in the number of propagation steps.

A rigorous von Neumann stability analysis, performed for the two-iteration ICN scheme and taking into account Eq. (13), results in an amplification factor equal to

$$\xi=\rho(\mathbf{I}+\Delta z\mathbf{A}_t+a_2\Delta z^2\mathbf{A}_t^2+a_1a_2\Delta z^3\mathbf{A}_t^3), \tag{19}$$

where $\rho(\mathbf{M})$ is the spectral radius of matrix $\mathbf{M}$, i.e., its maximum eigenvalue, which can be easily estimated. Hence, a stability criterion for the maximum step size Δz is derived by the constraint $|\xi|\leq 1$. For the reasonable choice $a_1=a_2=1/2$ it can be rigorously proven that the stability condition reduces to

$$\Delta z \leqslant \frac{2}{\rho(-j\mathbf{A}_t)}, \tag{20}$$

which is easier to estimate. To get a rough estimate for the maximum allowed step size in the ICN-FD-VBPM without extracting the matrix eigenvalues, we can employ a classical von Neumann stability analysis by considering a single spatial Fourier component and requesting that the amplification factor stay below 1. After some algebraic manipulations, we obtain the much simpler Courant-like approximate stability condition:

$$\Delta z \leqslant \min\left\{\left[\frac{1}{k_{\mathrm{ref}}}\left(\frac{1}{\Delta x^2}+\frac{1}{\Delta y^2}\right)-\frac{k^2-k_{\mathrm{ref}}^2}{4k_{\mathrm{ref}}}\right]^{-1}\right\}. \tag{21}$$

The analysis could be easily generalized for a number of n ICN iterations per step, following the pattern of Eq. (13) and the associated Eq. (19). After the algebraic manipulations for an arbitrary number of iterations, the amplification factor can be written in compact form as

$$\xi = \rho\left(\sum_{k=0}^{n+1}\left(\prod_{i=2}^{k} a_{n-i+2}\right)\Delta z^k \mathbf{A}_t^k\right). \tag{22}$$

In an analogous manner, it can be proved that the ICN scheme is unstable for a single iteration, conditionally stable for two or three iterations, unstable for four or five iterations, and so forth. This fact provides the rationale for the choice of the two-iteration ICN approach. Furthermore, for weight parameters $a_1=a_2=1/2$ it is easily proved that the ICN scheme is second-order accurate [14]. Other choices for a_1,a_2 may be useful for reinforcing stability or making the overall scheme more dissipative, at the expense of compromising second-order accuracy.

A series of numerical examples are presented in Section 4 to assess the accuracy and efficiency of the proposed ICN scheme, which will be hereinafter referred to as ICN-FD-VBPM. In addition, a comparison with other BPM methods is provided to establish the validity of our approach.

3. WIDE-ANGLE EXTENSIONS

The methodology developed in Section 2 refers to paraxial propagation. Although this is considered sufficient for an extended class of problems, there are application areas demanding a wide-angle treatment. Therefore, we present here a possible route toward such a generalization. In particular, wide-angle extensions are obtained by substituting Eq. (4) into Eqs. (3) without omitting the second-order derivative of the field envelope. In this respect, Eq. (5a) is written in general form as

$$-\frac{1}{j2k_{\mathrm{ref}}}\frac{\partial^2\tilde{\mathbf{E}}_t}{\partial z^2}+\frac{\partial\tilde{\mathbf{E}}_t}{\partial z}=\mathbf{A}_t\tilde{\mathbf{E}}_t, \tag{23}$$

which does not involve approximations of any kind. This can be considered a second-order algebraic equation with respect to the differential operator $\partial/\partial z$, which when solved results in the one-way (forward) parabolic equation

$$\frac{\partial\tilde{\mathbf{E}}_t}{\partial z}=jk_{\mathrm{ref}}(\mathbf{I}-\sqrt{\mathbf{I}+\mathbf{P}})\tilde{\mathbf{E}}_t, \tag{24}$$

where $\mathbf{P}=j2k_{\mathrm{ref}}^{-1}\mathbf{A}_t$. Owing to the nonlocal nature of the one-way operator, the corresponding matrix is dense, and an appropriate approximation of the square root operator has to be employed. Since we propose an explicit scheme, its nature has to be retained in the wide-angle extension, as well. The well-established framework of the rational Padé approximations is not applicable, as it inevitably leads to implicit formulations. We have circumvented this inherent difficulty by introducing a Taylor series approximation of the one-way operator [9]. Though it is understood that a Taylor series approximation is less accurate than to a rational (Padé) approximation of the same order, it is still an enhancement when compared with the paraxial approximation of Section 2. In particular, the square root operator is expanded in the vicinity of zero as

$$\sqrt{\mathbf{I}+\mathbf{P}}=\mathbf{I}+\frac{1}{2}\mathbf{P}-\frac{1}{8}\mathbf{P}^2+\frac{1}{16}\mathbf{P}^3+\cdots, \tag{25}$$

and Eq. (24) takes the form

$$\frac{\partial}{\partial z}\tilde{\mathbf{E}}_t=\mathbf{A}_t^{\mathrm{WA}}\tilde{\mathbf{E}}_t, \tag{26}$$

where

$$\mathbf{A}_t^{\mathrm{WA}}=-jk_{\mathrm{ref}}\left(\frac{1}{2}\mathbf{P}-\frac{1}{8}\mathbf{P}^2+\frac{1}{16}\mathbf{P}^3+\cdots\right). \tag{27}$$

If only the first term is retained, we obtain the paraxial scheme. Obviously there is no need for computing matrix powers, as already discussed in Section 2. Implementation of the wide-angle extension is similar to that in the paraxial case, at the expense of an increased number of matrix-vector multiplications per step. Other choices of the point about which the one-way operator is expanded or even alternative expansion types might be possible; however, such possibilities are beyond the scope of this first attempt toward a wide-angle extension, which is by no means an exhaustive treatment. It has to be noted that, although the maximum allowed step size dictated by the stability condition has to be reduced, the scheme is still applicable to typical practical problems.

4. NUMERICAL EXAMPLES

A. Multimode Interference Coupler

As a first example, we study a multimode interference (MMI) coupler [15] based on a deeply etched SiO_2 ridge waveguide. The main (wide) section of the device permits the propagation of many modes, excited by the field entering the MMI through the input waveguide. The different propagation constants of the excited modes and the respective interference result in the formation of multifold self-images of the input field at certain distances. The basic layout of the 1×4 MMI coupler under consideration is shown in Fig. 1(a), where $L_{\mathrm{MMI}}=245.5$ μm is the length and $W_{\mathrm{MMI}}=32$ μm is the width of the device. The cross-section of the input waveguide is given in Fig. 1(b), where

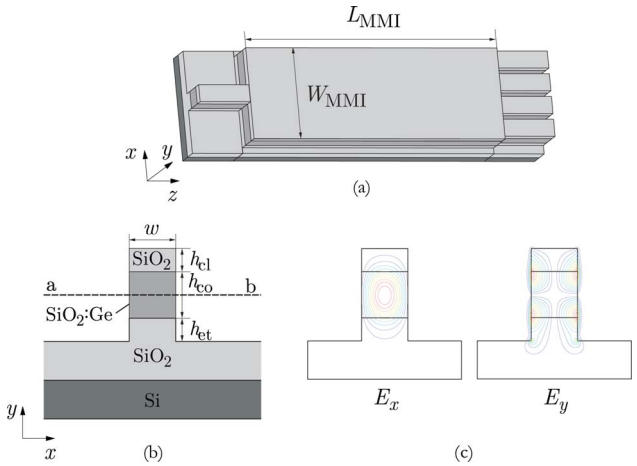

Fig. 1. (Color online) (a) Schematic layout of the 1×4 MMI coupler. (b) Cross-section of the deeply etched SiO_2 ridge input waveguide. (c) Fundamental x-polarized mode at $\lambda_0=1550$ nm. The minor field component has a maximum value equal to 3.7×10^{-3} when the maximum value of the major component is 1.

$h_{co}=6$ μm, $h_{cl}=3$ μm, $h_{et}=3$ μm, $w=6$ μm. The refractive index of the SiO_2 substrate is taken as $n_s=1.46$, and the refractive index contrast between the Ge dopped core and the substrate is $\Delta=0.75\%$. The geometrical features of the waveguide are selected according to [15], where an optimization technique was followed.

The BPM is an appropriate tool for the simulation of this type of device, which is characterized by extended cross-sections and appreciable propagation length. We have examined light propagation in the MMI coupler by employing the ICN-FD-VBPM presented in Section 2. The field exciting the device is the fundamental x-polarized mode of the input ridge waveguide at $\lambda_0=1550$ nm, Fig. 1(c), which is computed by the ICN-FD-VBPM in conjunction with the imaginary distance propagation technique [1]. Both the conventional CN and the ICN methods have been employed for this task for the purpose of comparison, and they yielded identical field profiles. In an attempt to further assess the ICN-FD-VBPM as a guided-mode solver, we have calculated the effective refractive index for the input waveguide. ICN yielded a value of 1.4633691772, which is in perfect agreement with the outcome of CN, found to be 1.4633691658. All subsequent simulations were performed on a 34×20 μm^2 transverse computational window, surrounded by uniaxial perfectly matched layer (PML) regions of 1 μm thickness for the absorption of outgoing waves. The transverse cell dimensions are $\Delta x=\Delta y=0.1$ μm, resulting in a total of 159,562 degrees of freedom, i.e., the unknown values of the transverse electric field at the nodes of the transverse grid. Hence, the total number of degrees of freedom is twice the number of grid nodes.

The field distribution of the dominant electric field component E_x over the length of the MMI coupler is presented in Fig. 2(a), illustrating the self-imaging of the input field and the field at the exit plane. The distribution of the dominant electric field component (E_x) at the exit face of the MMI is given in Fig. 2(b). To make a clear comparison of the solution obtained by the conventional CN and the explicit ICN methods, the field distribution on the output plane of the MMI coupler is shown in Fig. 3, plotted along the line ab, which runs parallel to the x axis [see Fig. 1(b)]. Moreover, a zoom to the peak of the curves is provided in a smaller window to facilitate assessing the effect

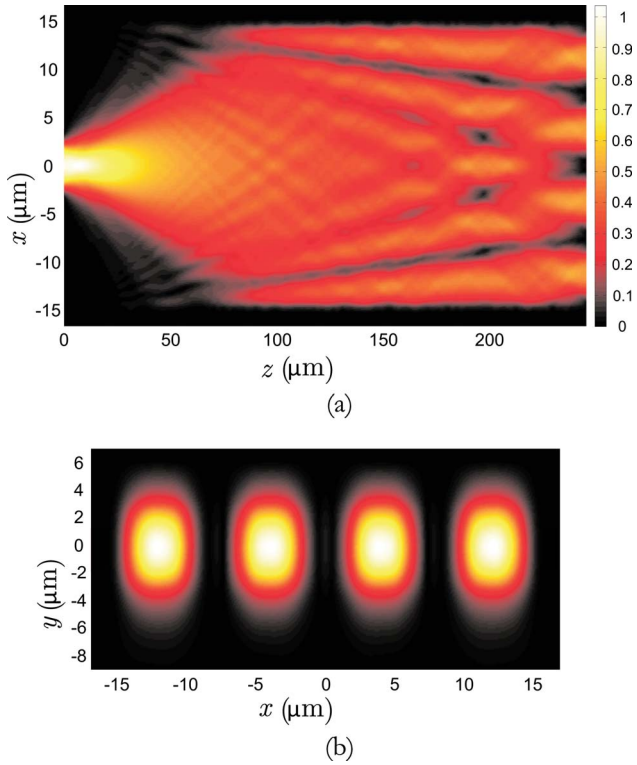

Fig. 2. (Color online) (a) Distribution of the dominant electric field component (E_x) over the whole extent of the MMI coupler, on the ab plane marked in Fig. 1(b). (b) Distribution of the dominant electric field component (E_x) on the exit plane of the 1×4 MMI coupler. Calculations were performed with the ICN-FD-VBPM.

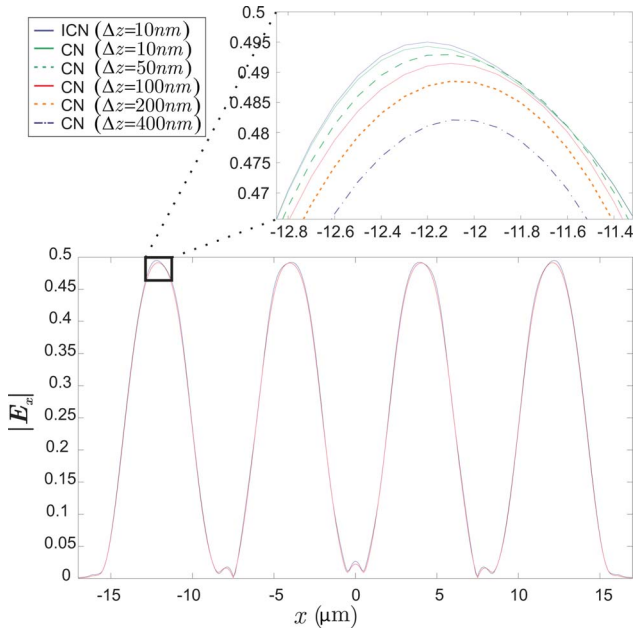

Fig. 3. (Color online) Variation of the dominant electric field component (E_x) along the ab line on the exit plane of the 1×4 MMI coupler. Calculations were performed with both the ICN-FD-VBPM and the conventional CN-FD-VBPM.

Table 1. Simulation Times for the MMI Coupler

	Axial Step Δz (μm)	Computation Time (s)
ICN-FD-VBPM (explicit)	0.01	1306
CN-FD-VBPM (implicit, iterative solver)	0.01	14363
	0.05	3759
	0.10	2434
	0.20	1751
	0.40	1532

of the axial step on the solution. As anticipated, the choice of a larger axial step leads to a reduction in the accuracy of the solution. It is emphasized that the ICN-FD-VBPM solution is virtually identical to the conventional CN-FD-VBPM for an axial step of $\Delta z = 0.01$ μm, which confirms the validity of the ICN approach.

Table 1 shows the computation time required on an Intel Core 2, 6400@2.13 GHz workstation for the conventional CN and the ICN case. All CN-FD-VBPM simulations were performed by setting the CN weight parameter equal to 0.51 and using an iterative solver (conjugate gradient squared). Owing to the nature and conditioning of the resulting FD matrices, such an approach appears to be the most economical in terms of computation time. We have tried a direct solver as well, which required an increase in execution time by approximately a factor of 5. Although the CN scheme allows larger propagation steps, this comes at the price of reduced accuracy. Considering the solution of either CN or ICN for the small step size of 0.01 μm as a reference, the ICN provides the correct solution at almost half the computation time of that required by the CN at 0.1 μm, while the latter further suffers a 1% maximum local error. The ICN performs even faster than the CN at $\Delta z = 0.4$ μm, which exhibits an error as high as 3%.

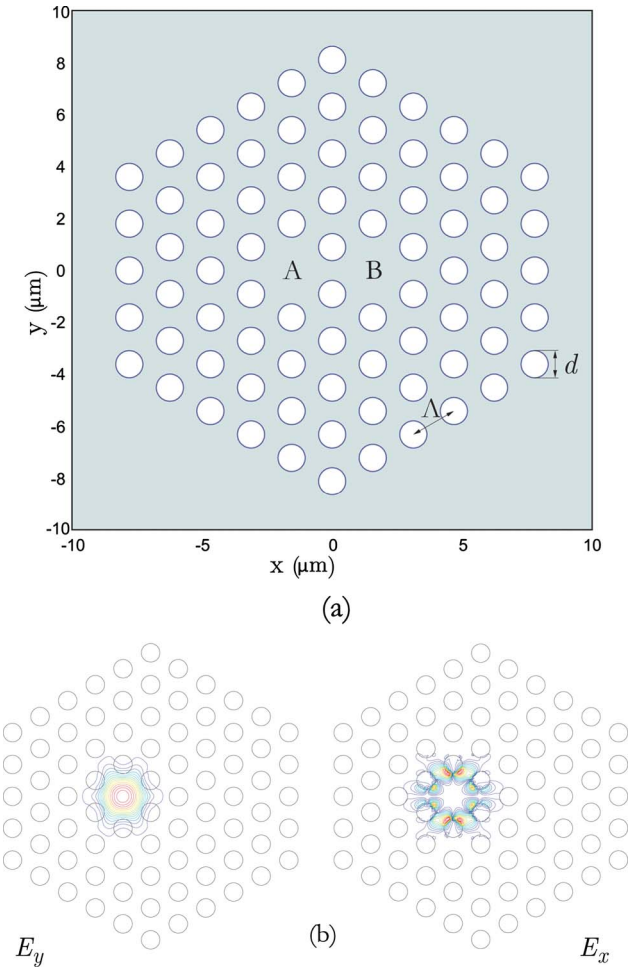

Fig. 4. (Color online) (a) Structural layout of a twin-core PCF coupler: Λ is the lattice constant, d is the cladding hole diameter. (b) Fundamental y-polarized mode of the single core waveguide at $\lambda_0 = 1550$ nm. The minor field component has a maximum value equal to 0.065 when the maximum value of the major component is 1.

B. Twin-Core Photonic Crystal Fiber Coupler

As a second example, we examine a twin-core photonic crystal fiber (PCF) coupler whose cross-section is illustrated in Fig. 4(a), following the design of coupler 4 in Table 2 of [16]. In a periodic triangular lattice of air holes on a silica background, two holes are missing, creating an index-guided twin-core PCF, which can be used as an optical directional coupler. The distance between adjacent cylinders (lattice pitch) of the periodic triangular cladding is $\Lambda = 1.8$ μm, the cladding's hole diameter $d = 0.58\Lambda$, and the refractive index of the silica fiberglass is taken equal to $n_g = 1.45$. The separation between the centers of the two cores, A and B, shown in Fig. 4(a) is $\sqrt{3}\Lambda$.

In order to quantify the optical properties of the PCF coupler, we launch the fundamental y-polarized mode of the corresponding single-core PCF at $\lambda_0 = 1550$ nm to core A, Fig. 4(b), and trace the evolution of the light along the z axis. For the subsequent simulations, a 20×20 μm^2 transverse computational window is used, including PML regions of 1 μm thickness. Since the PCF coupler cross-section is made of curved interfaces, for the sake of a better comparison we have also implemented a vectorial Crank–Nicolson finite-element BPM (CN-FE-VBPM) [4], using first-order edge elements for the transverse field and nodal elements for the axial component. This formulation is expected to provide a geometry-conforming discretization in the transverse plane while also serving as an accurate reference solution. In all FD-VBPM cases (ICN or conventional CN), transverse cell sizes of $\Delta x = \Delta y = 0.1$ μm are being employed, resulting in a total of 40,401 nodes and 80,802 degrees of freedom. In the case of the FE-VBPM the mesh consists of 38,729 nodes, which is very close to the number of nodes in the FD simulations, giving a total of 113,548 degrees of freedom.

As expected, the optical power periodically switches from core A to core B and vice versa. Figure 5 depicts the distribution of the E_y component at different propagation planes, illustrating the power exchange between the cores over the extent of one coupling length L_c. The power guided by core A versus the propagation distance z, calculated by the explicit ICN-FD-VBPM, is shown in Fig. 6 (blue curve). In the same graph, the values calculated by the CN-FE-VBPM and the conventional CN-FD-VBPM are presented with green and red curves, respectively. It

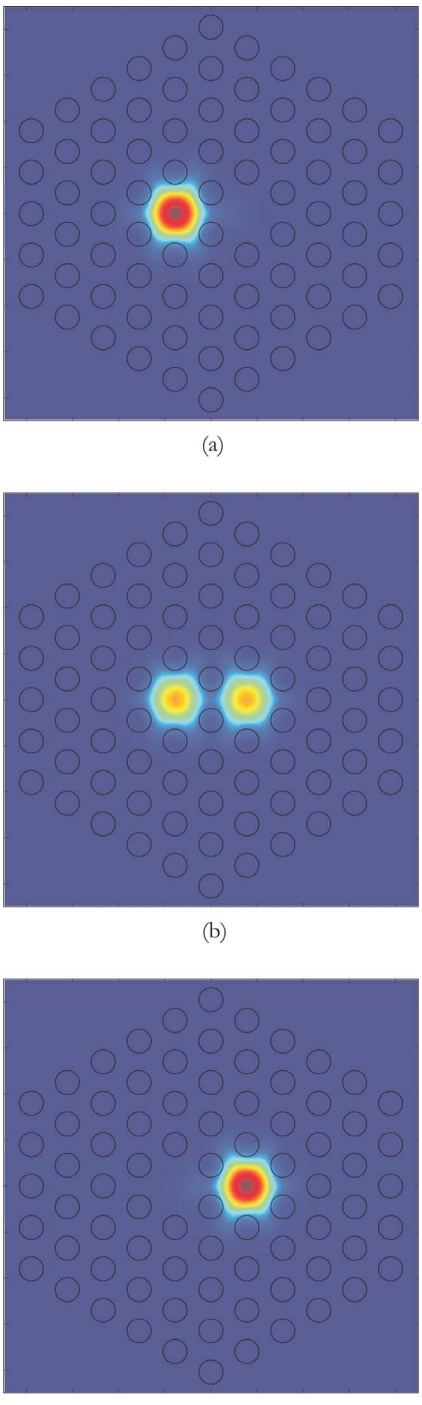

Fig. 5. (Color online) The y-polarized mode field distribution at (a) $z=0$ μm, (b) $z=L_c/2=147.25$ μm, (c) $z=L_c=294.5$ μm.

is important to point out that increasing the axial step Δz in the conventional CN-FD-VBPM leads to a concurrent increase in the numerical dissipation error, which degrades the solution. According to Fig. 6, the guided power is reduced to 97.6% and 96.1% of the input power at a propagation distance of $2L_c$ for $\Delta z=0.3$ μm and $\Delta z=0.5$ μm, respectively. The coupling length, as extracted from Fig. 6, and the computation time on an Intel Core 2, 6400@2.13 GHz workstation for each simulation approach are given in Table 2. The coupling length reported

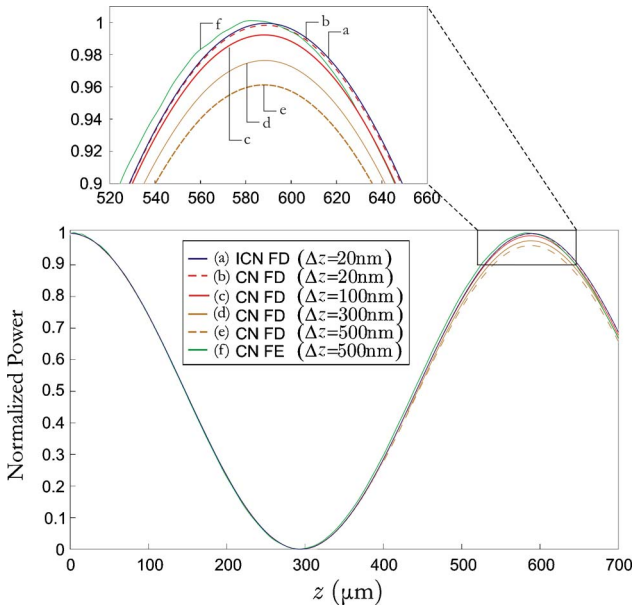

Fig. 6. (Color online) Guided power in core A versus propagation distance, calculated by the ICN-FD-VBPM, the conventional CN-FD-VBPM, and the CN-FE-VBPM.

in [16] for the same coupler is $L_c \approx 294$ μm, a value that compares favorably with our calculations.

It is observed that the ICN-FD-VBPM is significantly faster than the other approaches. Despite the staircasing effect, inevitable in FD discretizations, the results are satisfactory. Owing to the reduced step size, the ICN scheme is free from numerical dissipation, unlike the conventional CN scheme. Indeed, the ICN scheme requires at most half the time of the conventional CN-FD-VBPM, if the latter one is considered acceptable for a 4% error in transmitted power. For higher accuracy requirements, the ICN-FD-VBPM outperforms CN-FD-VBPM by a factor of 4 or more, according to Table 2. An iterative solver has been employed for the CN-FD-VBPM calculations for the reasons outlined in Subsection 3.A, whereas a direct solver seems to be the best choice for the CN-FEM-VBPM simulations. This is necessary because of the poor conditioning of the FEM matrices in vector formulations; an iterative solver will require substantially higher computation times.

Table 2. Simulation Times and Coupling Length for the Twin-Core PCF Coupler

	Axial Step Δz (μm)	Computation Time (s)	Coupling Length(μm)
ICN-FD-VBPM (explicit)	0.02	889	294.5
CN-FD-VBPM (implicit, iterative solver)	0.02	10904	294.5
	0.10	3340	294.5
	0.30	1797	294.5
	0.50	1486	294.5
CN-FE-VBPM (implicit, direct solver)	0.10	78878	292.5
	0.30	25996	292.5
	0.50	15662	292.5

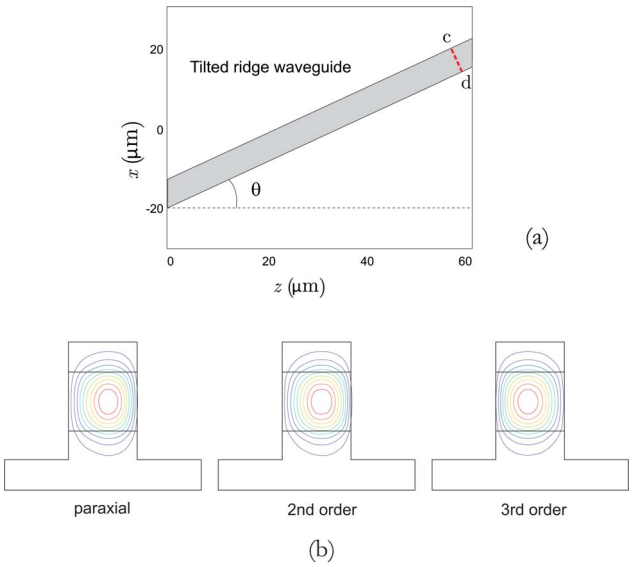

Fig. 7. (Color online) (a) Top view of the tilted ridge waveguide: the cross section is that of Fig. 1(b). (b) Dominant electric field component recorded on the *cd* plane for the paraxial, second-order wide-angle, and third-order wide-angle schemes.

C. Tilted Ridge Waveguide

We have repeated the calculations of Subsections 4.A and 4.B using the second-order wide-angle correction and obtained identical results, which confirms the essentially paraxial nature of these problems. Hence, to demonstrate the applicability of the proposed wide-angle extension, we consider the problem of a tilted waveguide, as shown in Fig. 7(a). The waveguide cross-section is the same as in Fig. 1(b), and the tilt angle is 30°. Both second- and third-order Taylor expansions have been implemented, and the corresponding results, together with the paraxial solution, are given in Fig. 7(b). It is evident that the paraxial solution suffers the higher distortion, as the mode is compressed to the inner side of the waveguide. This artifact is well anticipated, as the paraxial approximation tends to underestimate the angle of propagation. Although the second-order correction seems to alleviate this artifact, the third-order correction almost fully restores the mode profile. Taylor expansions were taken about zero, as is suggested by a theoretical assessment of the spectral bounds of the transverse operator. This decision was further backed by extensive numerical experimentation considering alternative expansion points, which confirmed the superiority of expansions about zero. In general, the third-order correction seems to be a fair tradeoff between accuracy and complexity.

5. DISCUSSION AND CONCLUSIONS

The development of explicit schemes for the VBPM is of key importance if one wishes to handle large-scale problems in photonics. This is evident, as the propagation operators are equivalent to sparse matrix multiplications, which are very economical in terms of processing power and memory management. In contrast, the well-established implicit schemes call for the solution of a sparse linear system per propagation step. If the problem size is moderate (in the range of few tens of thousands of unknowns in the transverse plane) then an implicit method is an appealing choice for the above task, owing to its high efficiency and robustness. For larger meshes and with the typical resources of a desktop workstation, one might prefer an explicit approach, since an implicit one is very commonly accompanied by reduced performance due to poor convergence of the linear system solver and also to the occurrence of other complications such as those originating from the absorbing boundary conditions used (for instance, PML). It is also not surprising that in a number of extreme cases, implicit methods may require considerably higher computation times or even fail completely. For all of the above reasons, avoiding the use of a sparse linear system solver, either direct or iterative, is of great benefit, provided of course that this is not at the expense of solution accuracy. This is exactly what is offered by our approach: a scheme that reproduces results identical to those of the conventional implicit VBPM (and thus is considered highly accurate), at a fraction of the computation time resulted by the implicit scheme. It also does not have the limitations that are inherent in sparse linear system solvers, thus allowing for handing millions of unknowns with virtually no difficulty. The efficiency of the ICN scheme is even more pronounced in the analysis of z-dependent structures, owing to the fact that a small axial step will be necessary to resolve the axial variation. In such a case, a scheme that generally provides the possibility of choosing larger step sizes, like the conventional CN, no longer offers any additional advantage.

REFERENCES

1. C. L. Xu, W. P. Huang, and S. K. Chaudhuri, "Efficient and accurate vector mode calculations by beam-propagation method," J. Lightwave Technol. **11**, 1209–1215 (1993).
2. W. P. Huang and C. L. Xu, "Simulation of 3-dimensional optical wave-guides by a full-vector beam-propagation method," IEEE J. Quantum Electron. **29**, 2639–2649 (1993).
3. Q. Wang, G. Farrell, and Y. Semenova, "Modeling liquid-crystal devices with the three-dimensional full-vector beam propagation method," J. Opt. Soc. Am. A **23**, 2014–2019 (2006).
4. D. Schulz, C. Glingener, M. Bludszuweit, and E. Voges, "Mixed finite element beam propagation method," J. Lightwave Technol. **16**, 1336–1342 (1998).
5. K. Saitoh and M. Koshiba, "Full-vectorial finite element beam propagation method with perfectly matched layers for anisotropic optical waveguides," J. Lightwave Technol. **19**, 405–413 (2001).
6. L. Vincetti, A. Cucinotta, S. Selleri, and M. Zoboli, "Three-dimensional finite-element beam propagation method: assessments and developments," J. Opt. Soc. Am. A **17**, 1124–1131 (2000).
7. Y. Chung and N. Dagli, "Analysis of z-invariant and z-variant semiconductor rib wave-guides by explicit finite-difference beam propagation method with nonuniform mesh configuration," IEEE J. Quantum Electron. **27**, 2296–2305 (1991).
8. Y. Chung, N. Dagli, and L. Thylen, "Explicit finite-difference vectorial beam propagation method," Electron. Lett. **27**, 2119–2121 (1991).
9. Y. C. Chung and N. Dagli, "A wide-angle propagation technique using an explicit finite-difference scheme," IEEE Photonics Technol. Lett. **6**, 540–542 (1994).
10. F. Xiang and G. L. Yip, "An explicit and stable finite-difference 2-d vector beam-propagation method," IEEE Photonics Technol. Lett. **6**, 1248–1250 (1994).

11. H. M. Masoudi and J. M. Arnold, "Spurious modes in the DuFort–Frankel finite-difference beam propagation method," IEEE Photonics Technol. Lett. **9**, 1382–1384 (1997).
12. P. Sewell, T. M. Benson, and A. Vukovic, "A stable DuFort-Frankel beam-propagation method for lossy structures and those with perfectly matched layers," J. Lightwave Technol. **23**, 374–381 (2005).
13. S. A. Teukolsky, "Stability of the iterated Crank–Nicholson method in numerical relativity," Phys. Rev. D **61**, 087501 (2000).
14. G. Leiler and L. Rezzolla, "Iterated Crank–Nicolson method for hyperbolic and parabolic equations in numerical relativity," Phys. Rev. D **73**, 044001 (2006).
15. Y. Shi and D. Dai, "Design of a compact multimode interference coupler based on deeply-etched SiO2 ridge waveguides," Opt. Commun. **271**, 404–407 (2007).
16. K. Saitoh, Y. Sato, and M. Koshiba, "Coupling characteristics of dual-core photonic crystal fiber couplers," Opt. Express **11**, 3188–3195 (2003).